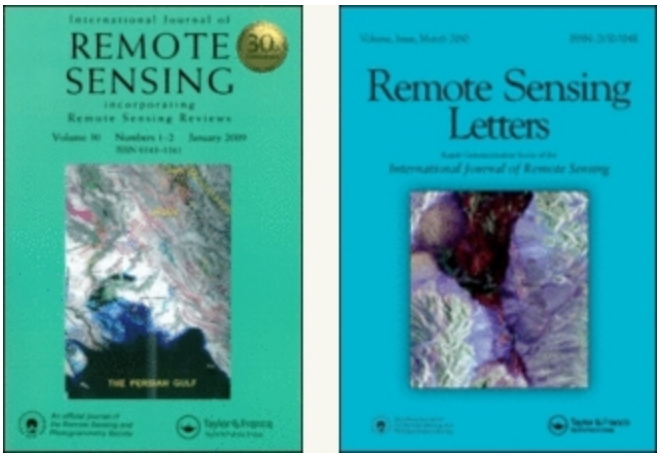

Multi-polarization C-band SAR imagery to quantify damage levels due to the Central Italy earthquake

Journal:	*International Journal of Remote Sensing*
Manuscript ID	TRES-PAP-2021-0249.R1
Manuscript Type:	IJRS Research Paper
Date Submitted by the Author:	06-May-2021
Complete List of Authors:	Ferrentino, Emanuele; Universita degli Studi di Napoli Parthenope Dipartimento di Ingegneria Nunziata, Ferdinando; Universita degli Studi di Napoli Parthenope Dipartimento di Ingegneria, Dipartimento di Ingegneria Bignami, Christian; INGV, National Earthquake Observatory Graziani, Laura; INGV, National Earthquake Observatory Maramai, Alessandra; INGV, National Earthquake Observatory Migliaccio, Maurizio; Universita degli Studi di Napoli Parthenope Dipartimento di Ingegneria; Istituto Nazionale di Geofisica e Vulcanologia
Keywords:	earthquakes, Polarimetric SAR, classification
Keywords (user defined):	

ARTICLE TEMPLATE

Multi-polarization C-band SAR imagery to quantify damage levels due to the Central Italy earthquake

Emanuele Ferrentino[a], Ferdinando Nunziata[a], Christian Bignami[b], Laura Graziani[b], Alessandra Maramai[b] and Maurizio Migliaccio[a,b]

[a]Dipartimento di Ingegneria, Università degli Studi di Napoli Parthenope, Napoli, Italy; [b]Istituto Nazionale di Geofisica e Vulcanologia, 00143 Rome, Italy

ARTICLE HISTORY
Compiled May 6, 2021

ABSTRACT
This study analyzes the ability of polarimetric Synthetic Aperture Radar (PolSAR) measurements to quantify post-earthquake damages. To reach this goal, a twofold task is addressed: on one side a processing chain, which exploits multi-polarization SAR features and a decision-tree classifier is proposed to quantify the levels of damage in earthquake-affected urbanized areas using dual-polarimetric (DP) SAR imagery. On the other side, a new damage index is developed that allows a fair spatial inter-comparison of building-by-building information, collected via ground surveys on the damaged areas, and SAR-derived damage maps. The proposed rationale is showcased using measurements related to the Central-Italy Earthquake occurred in 2016 where both Sentinel-1 DP imagery and ground-based information are available. Experimental results demonstrate the soundness of the proposed approach. The main outcomes can be summarized as follows: a) DP features perform better than single-polarization ones; b) DP features exhibit a larger sensitivity to lower damage grades if compared to the single polarization (SP) feature; c) the accuracy of the estimated damage levels depends on the requested granularity in the damage maps; d) the accuracy obtained using DP features spans from $\sim 52\%$ up to $\sim 71\%$ when 5 and 2 damage classes are considered, respectively.

KEYWORDS
PolSAR; earthquake; classification; change detection.

1. Introduction

Earthquakes are tremendous natural disasters that cause casualties and damages. Although the study of earthquake precursors is still an open matter and far away to be considered operational (De Santis et al. 2015), a fast damage assessment is an important step for post-disaster emergency response to reduce the impact of the disaster (Stramondo et al. 2006; Gong et al. 2016). Within this context, remote sensing plays an important role and the Synthetic Aperture Radar (SAR), due to its all-day and its almost all-weather fine spatial resolution imaging capabilities, can be very useful to observe damages caused by earthquakes. SAR methods are mainly based on single-polarization (SP) measurements and consist of exploiting the interferometric coherence and/or the normalized radar cross section (NRCS) measured on image

e-mail: emanuele.ferrentino@uniparthenope.it

pairs collected before and after the earthquake (Stramondo et al. 2006; Yonezawa and Takeuchi 2001; Matsuoka and Yamazaki 2004; Cihlar, Pultz, and Gray 1992; Hu and Ban 2014; Rignot and van Zyl 1993; Uprety, Yamazaki, and Dell'Acqua 2013). In (Yonezawa and Takeuchi 2001), a change detection analysis based on the interferometric coherence and the correlation between NRCS imagery collected before and after the 1995 Hyogoken-Nanbu (Kobe) earthquake in Japan is performed using the C-band European Remote-Sensing satellite ERS-1 SAR imagery. Experimental results show that the interferometric coherence decreases within the damaged areas identified using ground survey data collected after the earthquake. In (Matsuoka and Yamazaki 2004), the backscattering resulting from damaged urban areas is discussed using C-band ERS-1 SAR imagery and external building damage data obtained from a detailed field survey related to the 1995 Hyogoken-Nanbu earthquake. Results show a significant decreasing in the backscattering coefficient and a lower correlation between the pre– and post–event intensity images in areas severely damaged. In (Gamba, Dell'Acqua, and Lisini 2006), an approach based on the joint exploitation of pixel-based and feature-based information is proposed to detect damaged areas. Experiments, performed using Environmental Satellite (ENVISAT) Advanced SAR (ASAR) imagery collected over the city of Bam, Iran, during the earthquake occurred in 2003, show that the joint use of the two sources of information provides the best performance. In (Uprety, Yamazaki, and Dell'Acqua 2013) damages related to the Central Italy earthquake occurred in 2009 are analysed using very high resolution (VHR) TerraSAR-X HH-polarized SAR imagery and optical measurements acquired by QuickBird. The damage analysis, performed on a building basis, points out the benefits of SAR-observations to classify buildings damages of different levels.

To improve the performance of SAR-based methods in observing earthquake damaged areas, SAR measurements are often augmented with optical data (Stramondo et al. 2006; Gong et al. 2016; Romaniello et al. 2017; Brunner, Lemoine, and Bruzzone 2010). In (Stramondo et al. 2006) the urbanized areas damaged by the earthquakes occurred in 1999 and 2003 over the cities of Izmit, Turkey and Bam, Iran, respectively, are observed using C-Band ERS (Izmit) and ENVISAT-ASAR (Bam) SAR imagery and the joint combination of SAR and optical measurements collected by Indian Remote Sensing IRS1-C (Izmit) and the Advanced Spaceborne Thermal Emission and Reflection Radiometer (ASTER) (Bam). Experiments, which consist of combining pixel-based classification maps with ancillary ground surveys, show that the joint combination of SAR and optical measurements allow detecting 3 classes of damaged areas with an accuracy of 90%; while the accuracy decreased up to 60% when only SAR imagery are used. In (Gong et al. 2016), very high resolution (VHR) post-earthquake TerraSAR-X Staring Spotlight Imagery and original building footprint maps obtained from a combination of post-earthquake Laser Imaging Detection and Ranging (LIDAR) data and in situ investigation, are exploited to identify buildings destroyed by earthquakes. Then, machine learning classifiers are used to classify a building into damage classes. Experimental results, undertaken on the Wenchuan earthquake in China occurred on 12 May 2008, show that the method is able to distinguish between collapsed and standing buildings, with an overall accuracy of approximately 90%. In (Romaniello et al. 2017), X-band TerraSAR-X SAR imagery and optical measurements collected by GeoEye-1 are jointly used to observe damages related to the Haiti's earthquake. Two operational classifiers and ground based information are used to discuss the performance of damage maps. Experimental results, show that a 66% accuracy is achieved when only 3 damage levels are considered. The accuracy decreases up to 60% when using only SAR measurements.

Nowadays, the increasing number of spaceborne missions equipped with multi-polarization SAR triggered new added-value products in different domains (e.g.; land, forests, ocean, cryosphere and urban) (Lee and Pottier 2009). Within the urban domain, several studies have been proposed to exploit full-polarimetric (FP) SAR measurements to detect damages due to earthquake (Watanabe et al. 2012; Sato, Chen, and Satake 2012; Chen and Sato 2013; Park, Yamaguchi, and jin Kim 2013; Chen, Wang, and Sato 2016; Chen, Wang, and Xiao 2018; Zhai et al. 2016; Zhai and Huang 2016). Although FP SAR offers the largest amount of scattering information about the observed scene, hardware and budget considerations very often suggest the operational use of simpler polarimetric configurations, e.g.; the dual-polarimetric (DP) SAR (Nunziata, Migliaccio, and Li 2015; Buono et al. 2016). Only few studies have been proposed to exploit DP SAR measurements to observe urbanized areas damaged by earthquakes (Watanabe et al. 2016; Karimzadeh and Mastuoka 2017; Ferrentino et al. 2018, 2019). In (Watanabe et al. 2016) the interferometric SAR coherence is used to detect the damages due to the 2015 Gorkha (Nepal) earthquake. Experiments, undertaken using DP ALOS-PALSAR 2 L-band SAR imagery, show that the cross-polarized channel can help identifying damaged buildings with an accuracy around 35.1%. In (Karimzadeh and Mastuoka 2017) DP SAR data are exploited to discriminate between collapsed and preserved buildings, i.e.; a key information to perform damaged areas detection, after the 2016 Amatrice (Italy) earthquake. Both intensity and coherence features, evaluated using DP ALOS-PALSAR 2 L- and Sentinel-1 C-band SAR imagery, are exploited to show that cross-polarized channel can help identifying collapsed building with an accuracy around 84%. In (Ferrentino et al. 2018), the sensitivity of the inter-channel combination to earthquake-induced damages is investigated in DP SAR imagery collected by Sentinel-1 over the Central Italy earthquake. In (Ferrentino et al. 2019), the same data set is processed using a scattering-based change detector to emphasize damaged areas. Experimental results shot that the approach outperforms state-of-the-art ones in detecting damaged areas.

This study focuses on the quantitative analysis of earthquake-induced damages using DP SAR measurements and a properly processed ground information. The novelty of this study is twofold: on one side a processing chain that exploits dual-polarimetric SAR measurements to quantify the levels of damage is proposed; on the other side, a new index is developed that, based on a proper processing of ground-truth data collected via ground surveys in earthquake-affected area, allows a more consistent comparison with SAR-derived damage maps by providing the spatial distribution of damages by gorouping clusters of buildings. The processing chain ingests dual-polarimetric features (Ferrentino et al. 2018, 2019) in an unsupervised decision-tree classifier to generate a damage levels maps. The accuracy of SAR-based maps is discussed against polygonal-based ground truth and contrasted with a state-of-the-art benchmark SP method. Experimental results refer to the Central Italy earthquake occured in 2016 where both Sentinel-1 DP imagery and co-located ground information are available.
The remainder of the paper is organized as follows. In Section 2 the test site and the data set are discussed. In Section 3 the theoretical background is described; while experiments are shown and discussed in Section 4. Conclusions are drawn in Section 5.

2. Test site and dataset

The satellite data set consists of three single look complex (SLC) DP polarized SAR imagery collected before and after the 2016 Central Italy earthquake by the Copernicus Sentinel-1 mission over the area of Amatrice (Lazio, Italy) in ascending orbits, with an incidence angle of around 42° (see Table 1). The SAR scenes include the areas that resulted in the largest damages, i.e.: the towns of Amatrice, Norcia and Accumoli The vertically (V) polarized transmitted and received (VV) ground-projected excerpts of the SAR imagery collected before and after the earthquake over the area that includes the town of Amatrice (enclosed by the white dotted ellipse) are shown in Figure 1 (a) and (b), respectively.

The ground truth is provided by the Istituto Nazionale di Geofisica e Vulcanologia (INGV) Quick Earthquake Survey (QUEST) team and comes from a macro-seismic survey performed immediately after the event on the damaged area (Azzaro et al. 2016; Graziani et al. 2019). The QUEST team analysed the damages of each of the observed buildings according to the European Macroseismic Scale (EMS98) (Grünthal 1998). The latter distinguishes five damage classes (from negligible damages up to the destruction of the building).

3. Theoretical facts

This section introduces the theory that underpins the methodology proposed to contrast change maps derived by multi-polarization SAR with ground information obtained by ground surveys. Firstly, a new damage index is proposed that allows a fair inter-comparison with SAR maps by preserving the spatial distribution of damages. Secondly, the rationale that underpins the generation of damage maps from multi-polarization SAR imagery is described. Finally, the methodology to estimate damage levels from SAR maps is described.

3.1. *Definition of the weighted damage index (WDI)*

The field campaign provided a detailed building-by-building information on the damage grades. However, this information cannot be straightforwardly compared with SAR-derived maps for a twofold reason: on one side, the field campaign provides a building-by-building information whose spatial mapping into the SAR image plane is not straightforward. Hence, there is the necessity to define a single damage level that accounts for the changes observed in an area whose size can be actually observed in the SAR image plane. On the other side, EMS98 damage grades are not all detectable by SAR imagery which, in general, tend to underestimate actual damages. For instance, EMS98 damage grades 1 and 2 are expected to be hardly recognizable by SAR since they call for slight-to-moderate damages in the vertical structures of the buildings (e.g.; cracks). The only damages, belonging to this class, that may trigger the SAR detection are related to the fall of loose stones from the upper part of the buildings or the fall of brittle cladding and plaster. A damage of grade 3 results from both larger and extensive cracks and the detachment of roof tiles, chimneys fracture, buckling of reinforced rods and failure of individual infill panels hence, it is expected to be detectable by SAR. Finally, damages of grade 4 and 5 are expected to result in a well-distinguishable signature in the SAR imagery since they are related to very heavy structural damages, with partial structural failure of roofs and floors up to the

total collapse of building.
The above-mentioned discussion, together with the necessity to have a single damage value which accounts for all the EMS-98 grades surveyed, suggests developing a new damage index that we termed Weighted Damage Index (WDI):

$$\mathrm{WDI} = \sum_{k=1}^{N} (G_k \cdot P_k) \tag{1}$$

where $k = 1, ..., N$ stands for the $k-th$ polygon identified in the area of interest using the Global Urban Footprint (GUF) provided by the German Aerospace Center (DLR) (Esch et al. 2017). It must be noted that the polygon can refer to a whole municipality area or to a part of it. In this latter case, WDI is evaluated for the portion of the municipality area belonging to the selected polygon. G_k stands for the $k-th$ EMS98 damage grade; while P_k is the percentage of buildings belonging to the $k-th$ polygon that call for a damage G_k. In simple terms, WDI, whose values are bounded between 0 and 5, weights damage grades observed into cluster of buildings. Hence, WDI equal to 0 stands for undamaged building cluster; while WDI=5 stands for completely collapsed building clusters. The polygonal-based map of the earthquake-affected area is depicted in Figure 2 where the labels "1" to "5" refer to WDI. In conclusion, this index is expected to provide a fair way to intercompare SAR damage maps with damages observed via ground surveys by preserving also spatial information, i.e.; by linking the spatial distribution of the SAR-based damages with damage grades observed in the different clusters of buildings.

3.2. *Observing damages using DP SAR features*

The discussion related to section 3.1 clearly points out that not all the actual damages can be detected by SAR. Hence, SAR processing strategies that maximize the SAR sensitivity to damaged area are needed to improve damage detection. Within this context, a processing scheme based on the change detection is often adopted.
In this study, DP metrics are adopted and a new processing chain that consists of three steps is proposed to quantify damages, see block diagram of Figure 3. The first step is to pre-process DP SAR imagery by applying a 5×5 boxcar speckle filter and geocoding the SAR scenes. The second step consists of observing damaged areas using a change detection scheme that exploits a pair of DP SAR imagery collected before and after the earthquake. The third step consists of quantifying damage levels by processing the output of the multi-polarization features using an unsupervised decision-tree classifier. Then, the performance of the SAR-based outputs is contrasted with the WDI to assess the accuracy of the SAR driven damage maps. The theoretical background that relies on the basis of the multi-polarization features is here reviewed and the output of the features is first linked to the degree of damages affecting the built-up area, the last steps are addressed in the next subsection.

The observation of damages induced by the earthquake in the urbanized areas is performed using two DP metrics. The metric based on reflection symmetry (Ferrentino et al. 2018) is contrasted with a scattering-based change detector (Ferrentino et al. 2019; Ferrentino et al. 2020).
Reflection symmetry is a property well-known in scattering theory (Baum and Kritikos 1995; Cloude 2009). Accordingly, for every scatter at a given position, there is a

matching one in the reflected position about some axis (not necessarily aligned with the sensor's polarization coordinates). This property, which is satisfied by natural distributed scenes, is such that the coherence between co- and cross-polarized channels vanishes (Nunziata, Migliaccio, and Brown 2012):

$$\langle S_{\mathrm{VV}} S_{\mathrm{VH}}^{*} \rangle = \langle S_{\mathrm{HH}} S_{\mathrm{HV}}^{*} \rangle = 0 \tag{2}$$

Following this theoretical rationale, in (Ferrentino et al. 2018), a metric is proposed to detect earthquake-induced damages in DP SAR imagery collected over urbanized areas. The metric is based on the amplitude of the inter-channel correlation:

$$r = \left| \left\langle i_{x,x} i_{x,y}^{*} \right\rangle \right| \tag{3}$$

where i stands for the complex SAR imagery, $\{x, y\} = \{\mathrm{V}, \mathrm{H}\}$ and $|\cdot|$ stands for modulus.

The physical rationale can be summarized as follows. The reference scenario consists of the SAR imagey collected before the earthquake. In this case, the r metric (3) is expected to result in lower values when measured over natural scenarios (including forests, grasslands, crop fields, etc.). On the other side, larger values apply over areas that include man-made targets (e.g.; the urbanized area) since they call for deviations from the reflection symmetry property.

When dealing with the SAR imagery collected after the earthquake, departures from the reference scenario are expected over urbanized (man-made) areas which, due to the presence of damaged building, are expected to call for a more reflection symmetric behavior. In particular, the bigger are the damages, the lower are the expected r values.

Following this theoretical rationale, r is evaluated using a couple of SAR imagery collected before (r_{pre}) and after (r_{post}) the earthquake and the deviation of the r_{post} values from the reference r_{pre} ones is investigated to provide information on the levels of damage occurred in the urbanized areas. In fact, the deviation from the r_{pre} values measured over the urban area is expect to be correlated with the levels of damage. To provide a metric that quantifies the deviation of r_{post} from r_{pre}, the following feature is used:

$$\Delta r = \frac{r_{\mathrm{pre}} - r_{\mathrm{post}}}{r_{\mathrm{pre}} + r_{\mathrm{post}}} \tag{4}$$

Low Δr values (theoretically $\Delta r = 0$) are expected over urbanized areas not affected by the earthquake; while deviations from $\Delta r = 0$ are expected to correlate with the levels of damage.

The second DP metric relies on the Rayleigh's quotient

$$R(\boldsymbol{\omega}) = \frac{\boldsymbol{\omega}^{\dagger} \mathbf{C} \boldsymbol{\omega}}{\boldsymbol{\omega}^{\dagger} \boldsymbol{\omega}} \tag{5}$$

that consists of finding the scattering mechanism $\boldsymbol{\omega}$ that maximizes the scalar $R(\boldsymbol{\omega})$. This is a well-known problem in matrix algebra and it can be shown that if $\boldsymbol{\omega}$ is an eigenvector of $\mathbf{C}$, the extreme of $R(\boldsymbol{\omega})$ are related to the correspondent eigenvalues. Following this rationale, in (Ferrentino et al. 2019) a change detection metric is proposed that aims at maximizing the quadratic form associated to the difference between two covariance matrices collected before and after the earthquake:

$$\mathbf{C}_{\mathrm{CD}} = \mathbf{C}_2 - \mathbf{C}_1 \tag{6}$$

where $\mathbf{C}_1$ and $\mathbf{C}_2$ are the covariance matrices that refer to two DP SAR scenes collected before ($\mathbf{C}_1$) the earthquake and during the inter–seismic stage of the earthquake ($\mathbf{C}_2$).
Hence, maximizing $R(\boldsymbol{\omega})$ (5) when $\mathbf{C} = \mathbf{C}_{\mathrm{CD}}$ consists of solving the following eigenvalue problem (Ferrentino et al. 2019):

$$\mathbf{C}_{\mathrm{CD}}\underline{\boldsymbol{\omega}} = \lambda_i \underline{\boldsymbol{\omega}} \tag{7}$$

with λ_i being the $i-th$ eigenvalue with M=2 (3) when dual-polarimetric (quad-polarimetric) data are available. Note that, since $\mathbf{C}_{\mathrm{CD}}$ is no longer Hermitian and positive definite (HPSD), the eigenvalues can be also negative. Hence, the following metric is considered to detect earthquake-affected urbanized area (Ferrentino et al. 2019):

$$\lambda = \frac{1}{2}\sum_{i=1}^{M} |\lambda_i| \tag{8}$$

In this study, λ values are for the first time related to the level of damages occurred in the urbanized area. In fact, it is worth expecting that λ is correlated to the levels of damage, with low λ values associated to urbanized areas not affected by the earthquake; while larger λ values are expected to occur when dealing with collapsed buildings.

3.3. *Analysis of the damage level*

To analyze the levels of damage associated to the earthquake, a decision tree algorithm is applied to the outputs of the DP processing, see equations (4) and (8). The analysis aims at linking WDI levels to the output of the multi-polarization features. The classifier consists of contrasting the output of the multi-polarization features with thresholds. In this study, to match the reference ground truth (that consists of the 5 WDI classes depicted in Figure 2), 5 threshold (th) values are used to partition the output. To select th values, an optimization approach is proposed that consists of choosing the th values resulting in the best overall accuracy (OA) with respect to the ground information. The OA is measured using the confusion matrix that consists of

updating the diagonal elements when the damage level is correctly estimated or the off-diagonal ones when misclassifications occur.

The optimization procedure is first applied to a training area that, excerpted from the DP features, matches the ground truth enclosed in the dashed box of Figure 2 and includes 24 polygons and all of the 5 classes. The optimization procedure can be summarized as follows: 1) The 5 initial th values, bounded in the intervals $[0, 0.1]$ for Δr and $[0, 0.3]$ for λ, are selected for each multi-polarization feature. The upper bound of the intervals is chosen as the mean value of the metric evaluated over the damaged area. The selected values are such that the first and the last one coincide with the extreme of the interval, i.e.; ($th_0 = 0$, $th_4 = 0.1$) and ($th_0 = 0$, $th_4 = 0.3$) for Δr and λ, respectively. The remaining 3 th values are randomly selected in the reference interval. 2) The decision tree classifier is run with the selected 5 th values and OA is evaluated. 3) The 3 th values we left free to vary in the previous step, are incremented/decremented by $\Delta th = 10^{-3}$ until a maximum OA is reached, see Table 2. 4) The classification's score related to the training data set is listed in Table 3 where the parameters of the confusion matrix are listed for both r and λ. The calculation of the confusion matrix provides descriptive parameters: OA, producer accuracy (PA), user accuracy (UA), and kappa coefficient (K) (Jensen 2015). PA is the probability that a value in a given class is correctly classified; UA is the probability that a value predicted to be in a certain class really is that class; and OA measures how all the reference classes are correctly mapped. The K coefficient provides an overall analysis of the classification performance with respect to a reference random classifier. In particular, K < 0 (K $= 0$) stands for an accuracy that is worse (no better) than the one achieved using a random classifier, while when K tends to 1, the achieved accuracy is significantly better than the random classifier. In addition, in Table 3 is also listed a SP feature, namely the intensity correlation difference (ICD) (Romaniello et al. 2017), that is used for reference purposes. It can be noted that a satisfactory OA is achieved for both the DP features, with Δr and λ resulting in OA larger than 75% and 73%, respectively. The ICD feature calls for the worst result with an OA smaller than 40%. The K coefficient suggests the best performance is provided by Δr (K$>$ 64%), while K$>$ 63% when applies for λ. Again, the worst score is achieved by ICD (K$=$ 14%). The analysis of PA shows that the multi-polarization metrics exhibit a sensitivity to lower-grade damage levels better than the SP one. In general, all the metrics call for a performance that increases with increasing the damage levels, as expected. In conclusion, the extra-information carried on multi-polarization metrics plays a key role in improving the detection of lower-level damage grades.

Once the threshold values are available for the two DP features, the decision tree classifier is applied to the validation data set that consists of the whole scene (Quinlan 1986).

4. Experiment

In this section, experimental results obtained processing the SAR dataset augmented with auxiliary external ground truth information are discussed. First, damaged areas are observed using the DP features (4) and (8). Then, the levels of damage are quantified using decision-tree classifier applied to the whole SAR scene; finally, the accuracy of the levels of damage, estimated by DP SAR imagery, is discussed using the WDI map.

The first experiment is related to Δr and consists of processing the Sentinel-1 SAR

scene collected before (22 August 2016) and after (28 August 2010) the earthquake, see Figure 1 (a) and (b), respectively where an excerpt of the VV-polarized ground-projected SAR imagery is shown. The area includes the city of Amatrice (enclosed in the white dotted ellipse), and several smaller towns. By visually inspecting the squared-modulus SAR imagery related to the pre- and post-event, no well-distinguishable difference associated to the earthquake can be detected. This implies that a tailored processing is a mandatory step.

The output of the Δr (4) processing is depicted in Figure 4 (a) where, to focus on the urbanized areas affected by the earthquake, a masking is performed guided by the external ground truth polygons of Figure 2. By analyzing the image, one can note a granularity in the Δr values that confirms the correlation between Δr and the levels of damage and suggests different levels of damage both in the larger city of Amatrice and in the smaller towns. To better appreciate this granularity, a smoothing $N \times N$ window is applied with N=15 to reduce random variability. This N value is the one that optimises OA. The filtered output, depicted in Figure 4 (b), can be visually compared with the ground information depicted in Figure 2, noting a fairly good agreement in terms of variability of the levels of damage. To discuss the levels of damage in a quantitative way, the decision tree classifier is used. The map, classified at pixel level, is depicted in Figure 4 (c). The city of Amatrice is well zoned in terms of damage levels as well as many of the smaller towns. The accuracy of the SAR-based map is discussed against the WDI map using the confusion matrix calculated now at object (polygon) scale.

Indeed, to correctly compare the SAR-driven map with ground information that is provided on a polygonal basis, the former is converted into a polygonal-based map, see Figure 4 (d), using the polygons extracted from Figure 2 and considering, for each polygon, the mean value, rounded to the nearest integers towards infinity, of the damage levels of Figure 4 (c). The map of Figure 4 (d) shows a fairly good agreement with the ground information of Figure 2. The parameters of the confusion matrix, obtained contrasting pixel-by-pixel the map of Figure 4 (d) with the WDI map listed in Table 4, show a large superiority of Δr (∼49%) with respect to ICD (∼31%) confirming that the DP feature performs best in terms of OA. Δr still performs best when the K coefficient is considered. In fact, K is equal to $\sim$ 35% and $\sim$ 5% for Δr and ICD, respectively. Even in this case, PA (see Table 4) shows that DP information allows a better recognition of lower WDI levels with respect to SP information. To discuss the classification performance when SAR-driven maps characterized by a reduced granularity are available, classification results and ground information related to the classes 1 to 3 and 4 to 5 are grouped into two classes based on the assumption that higher levels of damage (1 to 3 grades in EMS98 corresponds to light damages, while 4 to 5 in EMS98 scale correspond to strong damage to completely destroyed buildings) are more detectable from satellite imagery, than un-damaged or very low damaged areas. This kind of information is expected to drive information on areas significantly affected by damages. The confusion matrix listed in Table 5 shows that better results are achieved in terms of OA although, at the except of a lower K coefficient. It must be also pointed out that, when reducing the number of classes, the DP feature performance slightly improves with respect to the SP one in terms of OA. This means that the richer information provided by polarization diversity plays a key role when finer granularity in the damage maps is needed.

The second experiment consists of processing λ in a fashion similar to what discussed in the previous experiment. The outputs of the λ processing are shown in Figure 5. The λ values related to the areas of interests are depicted in Figure 5 (a); while the smoothed values are shown in Figure 5 (b). Again, one can note a fairly good

agreement with the ground truth of Figure 2 in terms of variability of WDI levels. The damage levels map is depicted (at a pixel scale) in Figure 5 (c). The map shows a larger variability in terms of damage levels with respect to the r-based map of Figure 4 (c). The polygonal-based map depicted in Figure 5 (d) shows a fairly good agreement with the ground information of Figure 2. To quantitatively assess the classification performance against the WDI map, the confusion matrix is evaluated, see Table 4. It can be noted that λ scores better than Δr, performing best in terms of OA ($\sim$52%) and K ($\sim$37%). The analysis of PA confirms that λ performs better than ICD in observing all the damage levels. The performance, when the classification results and ground information related to the classes 1 to 3 and 4 to 5 are grouped in two classes, are listed in Table 5 where one can note that λ performs best achieving an OA and a K coefficient equal to 71% and 39.5%, respectively. This means that the scattering-based change detector exhibits a pronounced sensitivity even when the number of classes is reduced and a coarser granularity is needed.

5. Conclusion

In this study, multi-polarization SAR measurements are used to quantify post-earthquake damages. To achieve this goal, a twofold task is addressed: on one side a processing chain is introduced to quality damage levels from multi-polarization SAR imagery. On the other side, a new index termed as WDI is proposed that accounting for the change levels of clusters of buildings, allowing a fair comparison with the SAR-derived damage map. The processing chain consists of using DP SAR features to be ingested in a decision-tree classifier.

The performance of the damage level maps obtained processing Sentinel-1 DP SAR imagery collected over the area damaged by the 2016 Central Italy earthquake and using ground truth based on ground surveys and processed through the proposed WDI show the ability of DP SAR measurements to provide reliable information on the level of damages of urbanized areas. The main outcomes can be summarized as follows: a) DP metrics outperform the SP one in correctly identifying damage levels; b) DP metrics call for a sensitivity to lower damage levels better than the SP one that often results in a significant underestimation; c) the performance of the metrics depends on the number of damage level classes with an accuracy spanning from around 52% up to around 71%.

References

Azzaro, Raffaele, Andrea Tertulliani, Filippo Bernardini, Romano Camassi, Sergio Del Mese, Emanuela Ercolani, Laura Graziani, et al. 2016. "The 24 August 2016 Amatrice earthquake: macroseismic survey in the damage area and EMS intensity assessment." *Annals of Geophysics* 59.

Baum, C.E., and H.N. Kritikos. 1995. *Electromagnetic Symmetry*. Electromagnetics Library. Taylor & Francis.

Brunner, D., G. Lemoine, and L. Bruzzone. 2010. "Earthquake Damage Assessment of Buildings Using VHR Optical and SAR Imagery." *IEEE Transactions on Geoscience and Remote Sensing* 48 (5): 2403–2420.

Buono, A., F. Nunziata, M. Migliaccio, and X. Li. 2016. "Polarimetric Analysis of Compact-Polarimetry SAR Architectures for Sea Oil Slick Observation." *IEEE Transactions on Geoscience and Remote Sensing* 54 (10): 5862–5874.

Chen, S. W., and M. Sato. 2013. "Tsunami Damage Investigation of Built-Up Areas Using Multitemporal Spaceborne Full Polarimetric SAR Images." *IEEE Transactions on Geoscience and Remote Sensing* 51 (4): 1985–1997.

Chen, S. W., X. S. Wang, and M. Sato. 2016. "Urban Damage Level Mapping Based on Scattering Mechanism Investigation Using Fully Polarimetric SAR Data for the 3.11 East Japan Earthquake." *IEEE Transactions on Geoscience and Remote Sensing* 54 (12): 6919–6929.

Chen, S. W., X. S. Wang, and S. P. Xiao. 2018. "Urban Damage Level Mapping Based on Co-Polarization Coherence Pattern Using Multitemporal Polarimetric SAR Data." *IEEE Journal of Selected Topics in Applied Earth Observations and Remote Sensing* 1–11.

Cihlar, J., T. J. Pultz, and A. L. Gray. 1992. "Change Detection with Synthetic Aperture Radar." *International Journal of Remote Sensing* 13 (3): 401–414.

Cloude, S. 2009. *Polarisation: Applications in Remote Sensing*. OUP Oxford.

De Santis, A., G. De Franceschi, L. Spogli, L. Perrone, L. Alfonsi, E. Qamili, G. Cianchini, et al. 2015. "Geospace perturbations induced by the Earth: The state of the art and future trends." *Physics and Chemistry of the Earth* 85-86: 17 – 33.

Esch, Thomas, Wieke Heldens, Andreas Hirner, Manfred Keil, Mattia Marconcini, Achim Roth, Julian Zeidler, Stefan Dech, and Emanuele Strano. 2017. "Breaking new ground in mapping human settlements from space – The Global Urban Footprint." *ISPRS Journal of Photogrammetry and Remote Sensing* 134: 30 – 42.

Ferrentino, E., F. Nunziata, M. Migliaccio, and A. Vicari. 2018. "A Sensitivity Analysis of Dual-Polarization Features to Damage Due to the 2016 Central-Italy Earthquake." *International Journal of Remote Sensing* 0 (0): 1–18.

Ferrentino, E., F. Nunziata, H. Zhang, and M. Migliaccio. 2020. "On the Ability of PolSAR Measurements to Discriminate Among Mangrove Species." *IEEE Journal of Selected Topics in Applied Earth Observations and Remote Sensing* 13: 2729–2737.

Ferrentino, Emanuele, Armando Marino, Ferdinando Nunziata, and Maurizio Migliaccio. 2019. "A dual–polarimetric approach to earthquake damage assessment." *International Journal of Remote Sensing* 40 (1): 197–217.

Gamba, P., F. Dell'Acqua, and G. Lisini. 2006. "Change Detection of Multitemporal SAR Data in Urban Areas Combining Feature-Based and Pixel-Based Techniques." *IEEE Transactions on Geoscience and Remote Sensing* 44 (10): 2820–2827.

Gong, L., C. Wang, F. Wu, J. Zhang, H. Zhang, and Q. Li. 2016. "Earthquake-Induced Building Damage Detection with Post-Event Sub-Meter VHR TerraSAR-X Staring Spotlight Imagery." *Remote Sensing* 8 (11): 887–908.

Graziani, Laura, S. Mese, A. Tertulliani, Luca Arcoraci, Alessandra Maramai, and A. Rossi. 2019. "Investigation on damage progression during the 2016–2017 seismic sequence in Central Italy using the European Macroseismic Scale (EMS-98)." *Bulletin of Earthquake Engineering* .

Grünthal, G. 1998. *European Macroseismic Scale 1998 (EMS-98)*. 1st ed. Cahiers du Centre Européen de Géodynamique et de Séismologie, 15, Luxembourg.

Hu, H., and Y. Ban. 2014. "Unsupervised Change Detection in Multitemporal SAR Images Over Large Urban Areas." *IEEE J. Sel. Top. Appl. Earth. Obs. Remote Sens* 7 (8): 3248–3261.

Jensen, John R. 2015. *Introductory Digital Image Processing: A Remote Sensing Perspective*. 4th ed. Upper Saddle River, NJ, USA: Prentice Hall Press.

Karimzadeh, S., and M. Mastuoka. 2017. "Building Damage Assessment Using Multisensor Dual-Polarized Synthetic Aperture Radar Data for the 2016 M 6.2 Amatrice Earthquake, Italy." *Remote Sensing* 9 (4).

Lee, J.S., and E. Pottier. 2009. *Polarimetric Radar Imaging: From Basics to Applications*. Taylor & Francis.

Matsuoka, M., and F. Yamazaki. 2004. "Use of Satellite SAR Intensity Imagery for Detecting Building Areas Damaged Due to Earthquakes." *Earthquake Spectra* 20 (3): 975–994.

Nunziata, F., M. Migliaccio, and C. E. Brown. 2012. "Reflection Symmetry for Polarimetric

Observation of Man-Made Metallic Targets at Sea." *IEEE Journal of Oceanic Engineering* 37 (3): 384–394.

Nunziata, F., M. Migliaccio, and X. Li. 2015. "Sea Oil Slick Observation Using Hybrid-Polarity SAR Architecture." *IEEE Journal of Oceanic Engineering* 40 (2): 426–440.

Park, Sang-Eun, Yoshio Yamaguchi, and Duk jin Kim. 2013. "Polarimetric SAR remote sensing of the 2011 Tohoku earthquake using ALOS/PALSAR." *Remote Sensing of Environment* 132: 212 – 220.

Quinlan, J. R. 1986. "Induction of decision trees." *Machine Learning* 1 (1): 81–106.

Rignot, E. J. M., and J. J. van Zyl. 1993. "Change Detection Techniques for ERS-1 SAR Data." *IEEE Transactions on Geoscience and Remote Sensing* 31 (4): 896–906.

Romaniello, Vito, Alessandro Piscini, Christian Bignami, Roberta Anniballe, and Salvatore Stramondo. 2017. "Earthquake damage mapping by using remotely sensed data: the Haiti case study." *Journal of Applied Remote Sensing* 11 (1): 1 – 16.

Sato, M., S. W. Chen, and M. Satake. 2012. "Polarimetric SAR Analysis of Tsunami Damage Following the March 11, 2011 East Japan Earthquake." *Proceedings of the IEEE* 100 (10): 2861–2875.

Stramondo, S., C. Bignami, M. Chini, N. Pierdicca, and A. Tertulliani. 2006. "Satellite Radar and Optical Remote Sensing for Earthquake Damage Detection: Results from Different Case Studies." *International Journal of Remote Sensing* 27 (20): 4433–4447.

Uprety, Pralhad, Fumio Yamazaki, and Fabio Dell'Acqua. 2013. "Damage Detection Using High-Resolution SAR Imagery in the 2009 L'Aquila, Italy, Earthquake." *Earthquake Spectra* 29 (4): 1521–1535.

Watanabe, M., T. Motohka, Y. Miyagi, C. Yonezawa, and M. Shimada. 2012. "Analysis of Urban Areas Affected by the 2011 Off the Pacific Coast of Tohoku Earthquake and Tsunami With L-Band SAR Full-Polarimetric Mode." *IEEE Geoscience and Remote Sensing Letters* 9 (3): 472–476.

Watanabe, Manabu, Rajesh Bahadur Thapa, Tsuneo Ohsumi, Hiroyuki Fujiwara, Chinatsu Yonezawa, Naoya Tomii, and Sinichi Suzuki. 2016. "Detection of damaged urban areas using interferometric SAR coherence change with PALSAR-2." *Earth Planets Space* 68 (131).

Yonezawa, C., and S. Takeuchi. 2001. "Decorrelation of SAR Data by Urban Damages Caused by the 1995 Hyogoken-Nanbu Earthquake." *International Journal of Remote Sensing* 22 (8): 1585–1600.

Zhai, Wei, and Chunlin Huang. 2016. "Fast building damage mapping using a single post-earthquake PolSAR image: a case study of the 2010 Yushu earthquake." *Earth, Planets and Space* 68 (1): 86.

Zhai, Wei, Huanfeng Shen, Chunlin Huang, and Wansheng Pei. 2016. "Building Earthquake Damage Information Extraction from a Single Post-Earthquake PolSAR Image." *Remote Sensing* 8 (3).

Table 1. Sentinel–1 SAR data set

Acquisition date	Resolution (range× azimuth) (m)	Acquisition mode	Polarization	Angle of incidence (°)
10 August, 2016	2.33 × 13.92	Ascending	DP (VV+VH)	≈ 42
22 August, 2016	2.33 × 13.92	Ascending	DP (VV+VH)	≈ 42
28 August, 2016	2.33 × 13.92	Ascending	DP (VV+VH)	≈ 42

Table 2. Optimisation procedure

Step	Optimisation procedure
1	To select the 5 th values - th_0 and th_4 are constrained to be equal to the low and upper bounds of the feature values. - th_1, th_2 and th_3 are randomly selected in the internal of the feature values.
2	To run the decision tree algorithm and evaluating OA
3	To tune th_1, th_2 and th_3 and to iterate step 2-3 until a maxim OA is reached.

Table 3. Confusion matrix related to the training area and contrasted with the WDI map of Figure 2.

	UA (%)					PA (%)					OA (%)	K (%)
Feature \ WDI class	1	2	3	4	5	1	2	3	4	5		
Δr	0	100	82.8	69.8	75.95	0	45.9	77.7	59	92	75.13	64.2
λ	0	100	77.1	69.8	75.95	0	20.1	80.3	63.7	92.2	73.3	62.4
ICD	0	100	87.6	30.2	4	0	27.9	35	73.6	100	39.4	14

Table 4. Confusion matrix related to the 5 WDI classes obtained from the polygonal-based map.

	UA (%)					PA (%)					OA (%)	K (%)
Feature \ WDI class	1	2	3	4	5	1	2	3	4	5		
Δr	0	17.3	71.5	61.6	75.9	0	60	69.8	24.8	63.9	48.7	34.6
λ	0	17.3	84.7	55.5	75.9	0	34	57.9	38.5	65	51.7	36.8
ICD	0	9	69.2	39.3	3.6	0	22.8	30.3	34.5	37.3	30.6	4.8

Table 5. Confusion matrix related to two WDI classes obtained merging WDI classes 1 to 3 and 4 to 5.

	UA (%)		PA (%)		OA (%)	K (%)
Feature \ WDI class	1 (1-3)	2 (4-5)	1 (1-3)	2 (4-5)		
Δr	45.2	77.1	79.6	41.5	55.9	18.4
λ	70.3	72.2	83.4	55.1	71	39.5
ICD	79.1	22	66.8	34.7	59.9	1.2

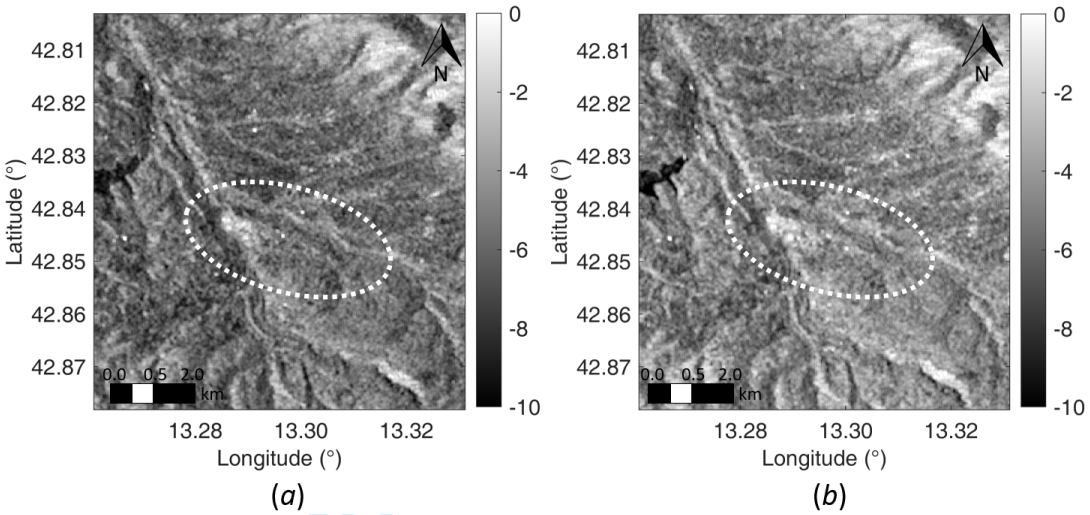

Figure 1. Excerpt of VV-polarized Sentinel-1 ground-projected SAR imagery collected in an ascending mode over the area of Amatrice, Italy: (a) before (22 August 2016) and (b) after (28 August 2016) the earthquake.

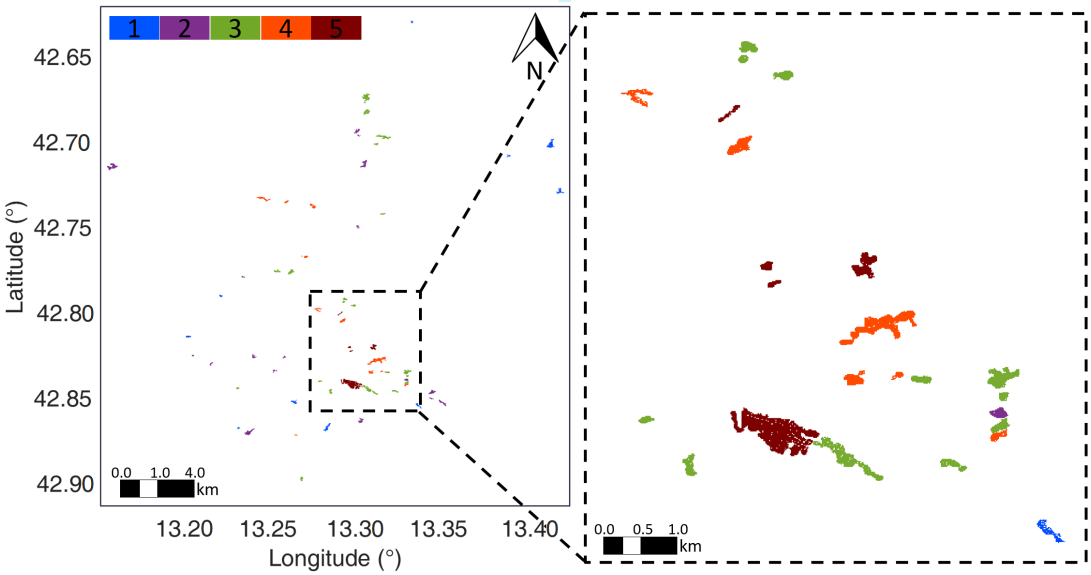

Figure 2. Polygonal ground truth obtained using the WDI scale. The labels 1 to 5 refer to the damage levels. On the bottom side of the image, an enlarged version of the area enclosed by the dashed black box is shown. This area is used to train the decision tree classifier.

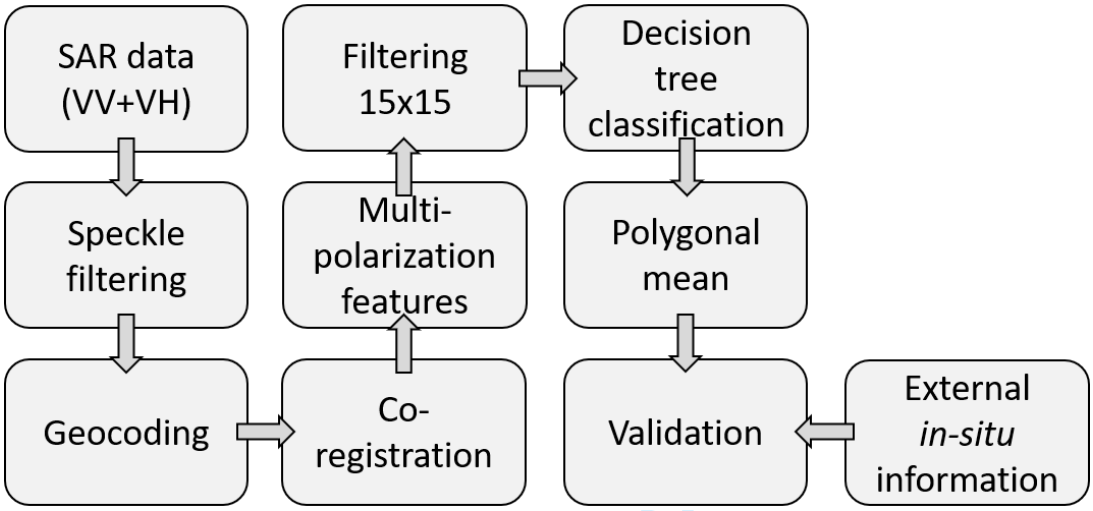

Figure 3. Block diagram of the earthquake damage classification scheme.

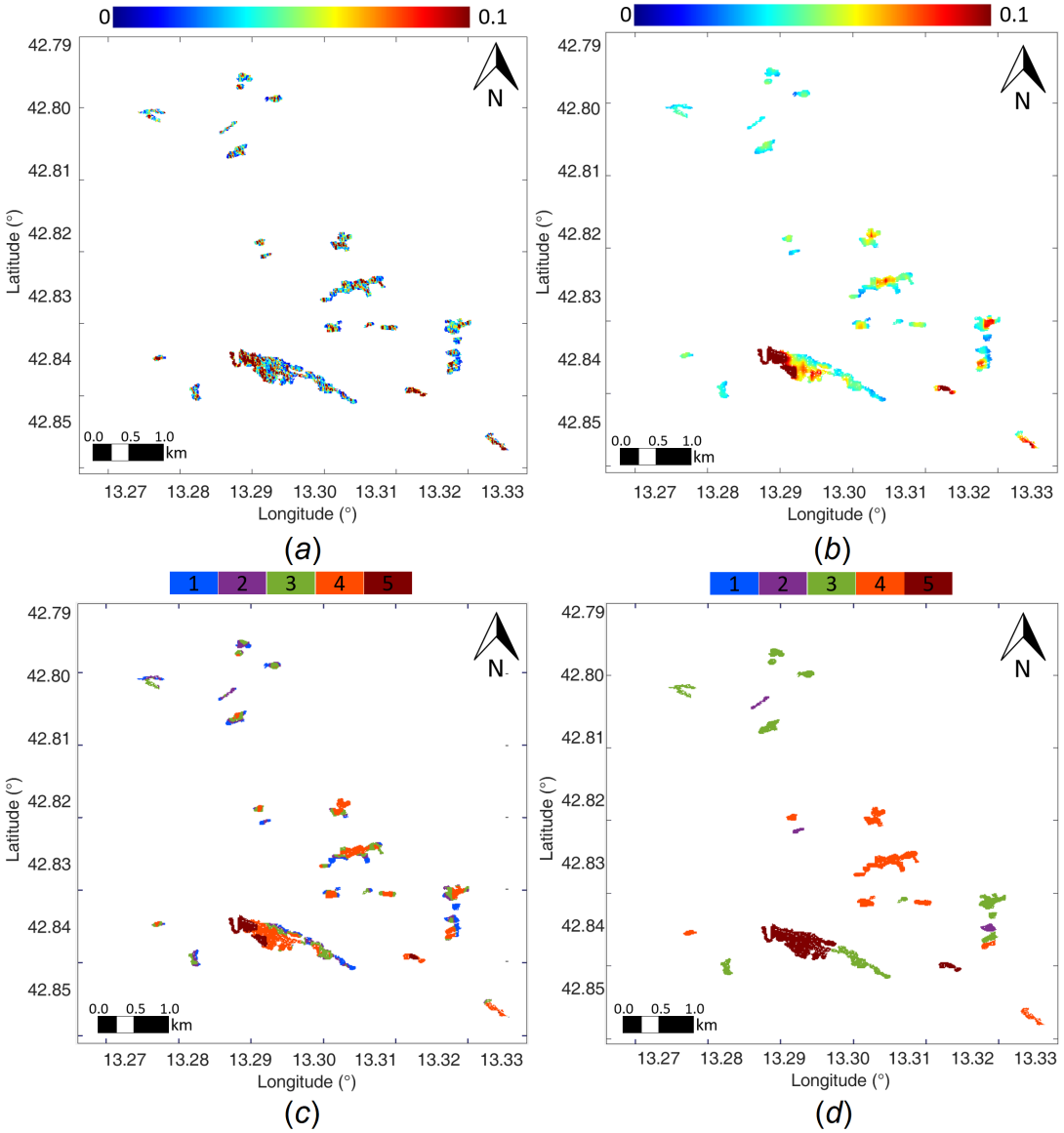

Figure 4. Unfiltered (a) and filtered (by a 15×15 pixel boxcar) (b) Δr values related to the damaged areas inspected using the ground truth of Figure 2. SAR pixel-based (c) and polygonal-based (d) damage maps obtained using the decision tree classifier.

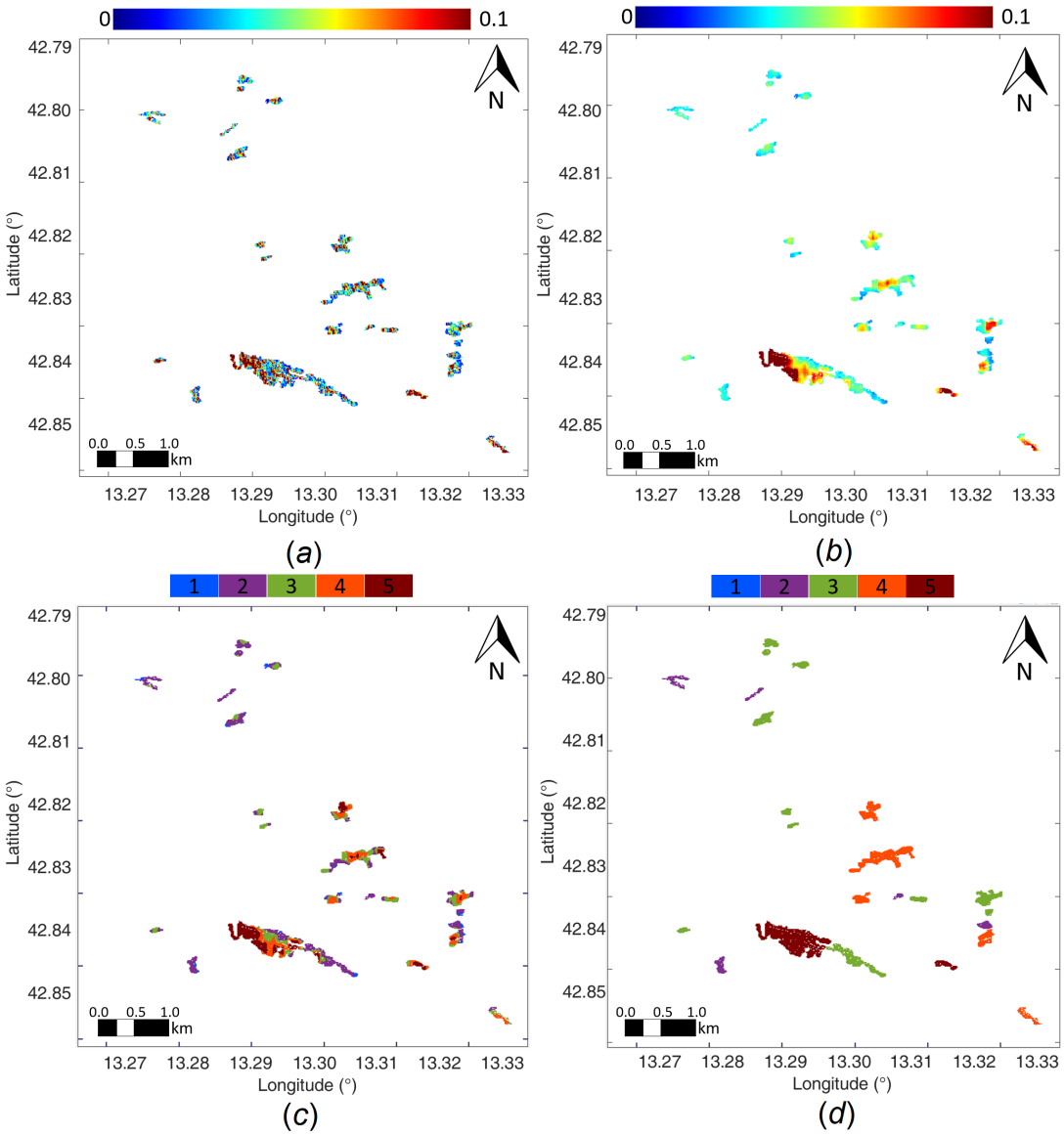

Figure 5. Unfiltered (a) and filtered (by a 15×15 pixel boxcar) (b) λ values related to the damaged areas inspected using the ground truth of Figure 2. SAR pixel-based (c) and polygonal-based (d) damage maps obtained using the decision tree classifier.